A Comprehensive Analysis and Control Strategy for Nullifying Negative- and Zero-Sequence Currents in an Unbalanced Three-Phase Power System Using Electric Springs

Kwan-Tat Mok, Siu-Shing Ho, Siew-Chong Tan, *Senior Member, IEEE*, and S. Y. (Ron) Hui, *Fellow, IEEE*

***Abstract*—This paper presents a general analysis and a control strategy that enables electric springs (ES) to mitigate the negative-sequence and zero-sequence currents in unbalanced three-phase power systems. The analysis indicates that under certain load conditions, power balance can be restored without the need for active power from the ES. Outside such conditions, the theory can pinpoint the precise operating point at which power balance can be achieved with the minimum active power from the ES. Thus, the optimum use of energy usage and battery size for providing/storing active power can be realized. Simulation and experiment results obtained from a 3-kW hardware setup have verified the new theory and the control method.**

***Index Terms*—Electric springs (ESs), neutral current, negative-sequence currents, power imbalance, radial-chordal decomposition, symmetrical components.**

I. Introduction

POWER flow imbalance among different power phases is a general phenomenon in three-phase ac power utility grids. Such power imbalance can be classified as short term and long term [1]. For short-term imbalance, unbalanced currents are relatively larger than those of the long-term ones. They are caused by unsymmetrical faults such as the phase-to-neutral short circuit in power lines and equipment failures [1]. If these large unbalanced currents are not properly handled, generator trips can occur [2]. For long-term imbalance, unbalanced currents are typically milder (smaller amplitude). They are generated by an uneven distribution of loadings on different power phases [1], [3], [4]. These unbalanced line currents can cause severe disturbance to induction machines [5], excessive flows of neutral currents [6], significant power losses [7], reduction in system's efficiency [8], low power factor [8], and severe reactive power burdens [8]. Furthermore, over the past decades, there is an increasing use of nonlinear loads, such as adjustable speed drives, computer power supplies, and asynchronous ac–dc–ac links [4], [8]. As a result, both of system power balance and power quality are adversely affected.

Many solutions have been proposed to resolve the issue of long-term power imbalance and other power quality related issues such as power factor degradation and current/voltage harmonic contaminations. These solutions can be classified into following four types:

1) transformers and synchronous condensers;
2) passive filters (PFs);
3) active filters (AFs);
4) hybrid filters (HFs).

Conventional devices, such as synchronous condensers and transformers with tap changers, have been used to address power quality issues [3], [9]. The drawbacks of these methods are their large physical size, heavy weight, and high maintenance cost [3], [6]. The installation of PFs, such as fixed capacitor banks and *LC* filters, are alternative solutions [5], [8], [10], [11]. However, PFs are incapable of eliminating random and time-varying harmonic pollution that is generated from solid-state controlled devices. In this respect, a fast dynamic and adaptive solution such as the AFs is required [12]–[17]. In general, AFs can be connected in either series or in parallel with the power network. The static var compensator (STATCOM) and the static synchronous series compensator (SSSC) are typical examples of shunt-type (parallel) and series-type AFs, respectively [12], [13]. The combination of AFs and PFs forms the HFs (e.g., the unified power flow controller (UPFC) is formed by combining a STATCOM and an SSSC coupled by a common dc link [15]). Another example of HFs is a STATCOM connected in series with an inductor [16]. The reasons for the use of HFs are to improve the dynamic performance and to reduce the size of filter devices [4].

Although the aforementioned techniques can achieve substantial improvements on different aspects of power quality issues in conventional power networks, the new challenges arising from emerging power grids pose an entirely different set of problems that are not resolvable through these techniques and that should be handled by new solutions. Increasing use of intermittent renewable energy could lead to instantaneous imbalance be-

Manuscript received May 16, 2016; revised October 11, 2016; accepted November 21, 2016. Date of publication December 6, 2016; date of current version May 9, 2017. This work was supported by the Hong Kong Research Grant Council under the theme-based project T23-701/14-N. Recommended for publication by Associate Editor Prof. J. M. Guerrero.

K.-T. Mok, S.-S. Ho, and S.-C. Tan are with the Department of Electrical and Electronic Engineering, The University of Hong Kong, Hong Kong (e-mail: barrymok@connect.hku.hk; ssho@eee.hku.hk; sctan@eee.hku.hk).

S. Y. R. Hui is with the Department of Electrical and Electronic Engineering, The University of Hong Kong, Hong Kong, and also with the Department of Electrical and Electronic Engineering, Imperial College London, London SW7 2AZ, U.K. (e-mail: ronhui@eee.hku.hk).

Color versions of one or more of the figures in this paper are available online at http://ieeexplore.ieee.org.

Digital Object Identifier 10.1109/TPEL.2016.2636226

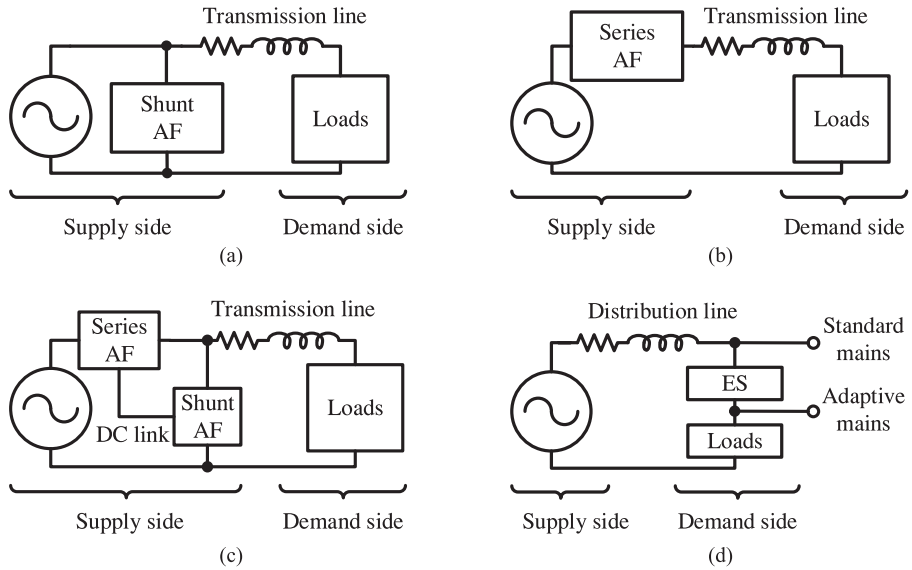

Fig. 1. Illustration of a power system with different technology installed. (a) Shunt-type active filter. (b) Series-type active filter. (c) Hybrid filter. (d) Series-type electric spring.

tween power supply and demand, which is a key factor for grid voltage amplitude and frequency fluctuations [18]. Electric springs (ES) have been proposed to resolve this imbalance issue, and simultaneously, serve to perform conventional power-quality improvement functions [6], [19]–[21]. The first version of ES has been initially proposed for grid voltage stabilization through reactive power compensation and active power control of a non-critical (NC) load. This ES is configured by a voltage source converter that is connected in series with an NC load (such as an electric heater) [19]. The second version of ES includes battery storage for providing both active and reactive power compensations [20]. These two versions of ES are defined as series-type ES. Further research works have been conducted on using ES for power factor correction [20], harmonic compensation [21], and neutral current mitigation [6].

Fig. 1(a)–(d) shows the simplified block diagrams of a shunt-type AF, a series-type AF, an HF, and a series-type ES, respectively. The supply-side voltage in each of these figures represents the upstream part of the power network. That can be the output of the step-up transformer inside a power generation plant [in the cases of Fig. 1(a)–(c)] or the output of the step-down transformer of the distribution substation [in the case of Fig. 1(d)]. The loads in the figures represent the combination of the loads at the demand side. ESs are different from traditional flexible ac transmission system (FACTS) devices by 1) using an input-voltage control to regulate the standard mains and 2) providing an adaptive mains for NC loads. Unlike the traditional AFs that are the large-scale infrastructures and are installed at transmission levels, the ES are small power-electronic devices and are targeted to be installed at distribution levels. They can be distributed over the distribution network to form a distributed active suspension system. Since ES can dynamically modulate the NC load power, they form a distributed demand-response solution to balance the power supply and demand.

Some preliminary work on the reduction of power imbalance using ES was reported in [6]. Due to the lack of a systematic analysis, previous work obtained near-optimum solutions based on genetic algorithm (GA) to reduce neutral current in a three-phase power system. Other important power imbalance issues (such as negative-sequence and zero-sequence currents, and optimum power compensation and battery capacity) remain unsolved. Excessive negative-sequence current can affect the reliability of power systems [1], [2], [22], [23]. For instance, in the direct-and-quadrature (*dq*) control commonly adopted in power compensators, the presence of negative-sequence components can cause the *dq* variables to vary at twice the fundamental grid frequency [22]. Hence, the compensation algorithm for power balancing would not work well because of calculation errors introduced by such variations [23]. European Standard EN 60034-1 has been initiated to govern the acceptable negative-sequence currents in synchronous machines [24].

In this paper, a comprehensive analysis on the use of ES for reducing power imbalance in a three-phase system is presented. It provides a new theoretical platform to work out the precise control strategy and analytical solution for a series-type three-phase ES in order to reduce both zero-sequence and negative-sequence currents in an unbalanced power system. Under certain conditions, this method can reduce system power imbalance without requiring real power from the ES. Beyond such conditions, the theory can pinpoint the precise condition at which the minimum active power is required from the ES to restore power balance. Therefore, the battery storage on the dc link of the ES can be minimized. Simulation and experiment results obtained from a 3-kW prototype are included to validate the proposed method.

II. Three-Phase Power Balancing via ESs

Three-phase power imbalances can be commonly found in large residential buildings [25], of which the general electrical system diagram is shown in Fig. 2. The system can be divided into three sections, namely the supply-side section, the centralized-load section, and the single-phase residential-load section. In the supply-side section, the building acquires power

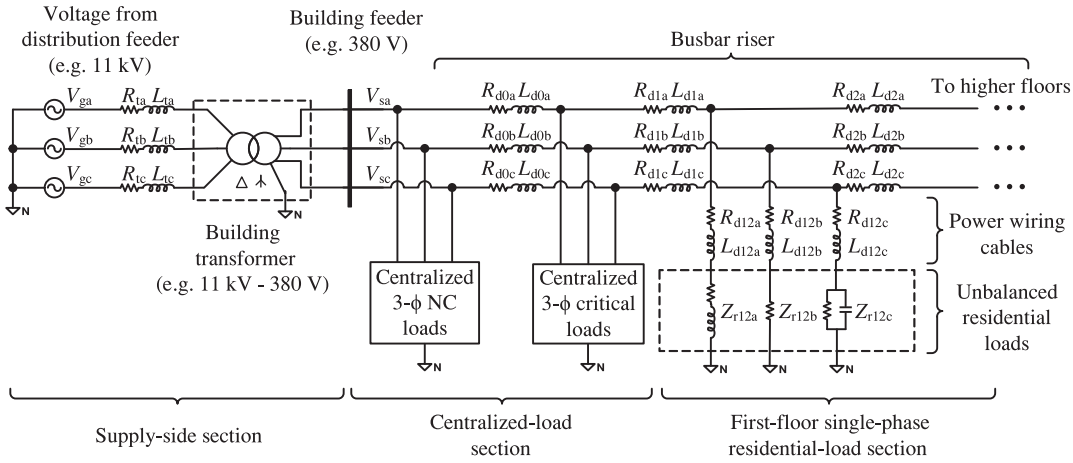

Fig. 2. General electrical system diagram of a large residential building.

from a distribution feeder. The distribution voltage is stepped down to the utility level via a building transformer and its output voltage is denoted as the building supply voltage V_{si} on phase i, where $\mathrm{i} = \mathrm{a}, \mathrm{b}$, or c. The centralized-load section consists of three-phase electrical devices, such as lifts, escalators, central air-conditioning systems, and central water heaters. The single-phase residential-load section involves loads fed by individual phases. Power consumptions among different phases are usually not identical. Since the power supply units of centralized three-phase loads are generally close to the building transformer, their associated parasitic impedances are ignored in this analysis.

The centralized three-phase loads can be categorized into critical loads and NC loads. Critical loads are fed by the standard ac mains (V_{sa}, V_{sb}, V_{sc}) tightly regulated through an input-voltage control loop by the ES. Examples are lifts and escalators. The ES also provides an adaptive ac mains (V_{oa}, V_{ob}, V_{oc}) with a higher tolerance of supply voltage for the NC loads. A centralized three-phase water heating system can be considered as an NC load.

In this section, a comprehensive steady-state analysis of using an ES for restoring power balance in a three-phase power system is presented. A simplified block diagram of the electric system with an ES installed in a residential building is shown in Fig. 3. It is assumed that the three-phase supply voltage of the building is constant and balanced, of which the root-mean-square (RMS) magnitude of the voltage is denoted as

$$|V_{\mathrm{s\_Ref}}| = |V_{\mathrm{sa}}| = |V_{\mathrm{sb}}| = |V_{\mathrm{sc}}|. \tag{1}$$

The NC load (e.g., a centralized water heater) on phase i can be represented by a complex impedance $Z_{\mathrm{oi}} = R_{\mathrm{oi}} + jX_{\mathrm{oi}}$. The other impedances of the building on phase i, including 1) the critical three-phase loads; 2) the parasitic impedances of the busbar riser; and 3) the impedances of devices in all domestic electric loads, are combined together and are represented by a branch complex impedance $Z_{\mathrm{bi}} = R_{\mathrm{bi}} + jX_{\mathrm{bi}}$. Note that the impedance of the centralized water heater can be assumed to be purely resistive R_{oi}. Nevertheless, a complex impedance form Z_{oi} will be used in this analysis to prevent the loss of generality as different types of loads with complex impedance are applicable as an NC load [20]. Under this configuration, the complex power of the whole building (S_{sa}, S_{sb}, S_{sc}) consists of two parts: 1) the complex power consumed by the ES-associated smart load (S_{sla}, S_{slb}, S_{slc}); and 2) the complex power consumed by the branch loads (S_{ba}, S_{bb}, S_{bc}) as highlighted in Fig. 3. Considering the situation that the ES is not activated. The voltage of the adaptive ac mains is equal to that of the standard ac mains. The smart-load complex power of phase i can be expressed as

$$S_{\mathrm{sli}} = S_{\mathrm{nom\_sli}} = P_{\mathrm{nom\_sli}} + jQ_{\mathrm{nom\_sli}} = V_{\mathrm{si}}\frac{\overline{V_{\mathrm{si}}}}{\overline{Z_{\mathrm{oi}}}} \tag{2}$$

where $S_{\mathrm{nom\_sli}}$ is defined as the nominal value of S_{sli}. The branch complex power on phase i is

$$S_{\mathrm{bi}} = P_{\mathrm{bi}} + jQ_{\mathrm{bi}} = V_{\mathrm{si}}\frac{\overline{V_{\mathrm{si}}}}{\overline{Z_{\mathrm{bi}}}}. \tag{3}$$

Hence, the three-phase nominal power of the building (with the ES deactivated) $S_{\mathrm{nom\_s}}$ is

$$S_{\mathrm{nom\_s}} = S_{\mathrm{nom\_sl}} + S_{\mathrm{b}} \tag{4}$$

where $S_{\mathrm{nom\_sl}} = S_{\mathrm{nom\_sla}} + S_{\mathrm{nom\_slb}} + S_{\mathrm{nom\_slc}}$ and $S_{\mathrm{b}} = S_{\mathrm{ba}} + S_{\mathrm{bb}} + S_{\mathrm{bc}}$ are the three-phase nominal smart-load complex power and the three-phase branch complex power of the building, respectively (see Fig. 3). Consider the situation that the ES is activated and that it can deliver a certain ES voltage on each phase such that the system operates to behave as a load that consumes a balanced three-phase power. The balanced per-phase active and reactive power of the building are denoted as $P_{\mathrm{s\_bal}}$ and $Q_{\mathrm{s\_bal}}$, respectively. Thus, $P_{\mathrm{sa}} = P_{\mathrm{sb}} = P_{\mathrm{sc}} = P_{\mathrm{s\_bal}}$ and $Q_{\mathrm{sa}} = Q_{\mathrm{sb}} = Q_{\mathrm{sc}} = Q_{\mathrm{s\_bal}}$. The active and reactive branch power (P_{bi} and Q_{bi}) are unchanged and (3) remains valid after the activation of the ES because the supply voltage level is remained at $|V_{\mathrm{s\_Ref}}|$. In this balanced system, the smart-load active power ($P_{\mathrm{sli}} = P_{\mathrm{s\_bal}} - P_{\mathrm{bi}}$) and reactive power ($Q_{\mathrm{sli}} = Q_{\mathrm{s\_bal}} - Q_{\mathrm{bi}}$) on phase i can be expressed by using the power conservation analysis. Thus, the smart-load apparent power on phase i can be expressed as

$$|S_{\mathrm{sli}}| = \sqrt{(P_{\mathrm{s\_bal}} - P_{\mathrm{bi}})^2 + (Q_{\mathrm{s\_bal}} - Q_{\mathrm{bi}})^2}. \tag{5}$$

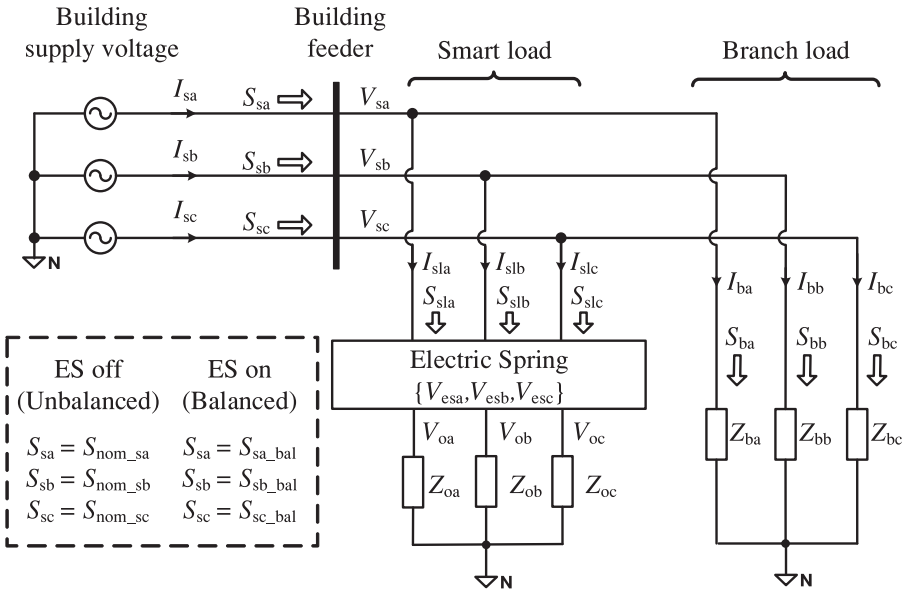

Fig. 3. Simplified electrical diagram of a large residential building.

The operating voltage of the ES on each phase has to be determined according to the power requirement described in (2)–(5). The calculation of the ES voltage can be a tedious process if an improper mathematical approach is adopted. Unlike [6] in which GA is adopted to estimate the numerical results (in order to avoid the solving of complex equations), the analysis here is based on the radial-chordal decomposition (RCD) method [26]. It can provide the precise analytical solution to achieve power balance. The RCD method decomposes the ES voltage into radial and chordal subcomponents such that the power angle and the power magnitude of the ES-associated smart load can be independently controlled. According to [26, eqs. (20) and (21)], the power amplitude (apparent power) of the ES-associated smart load and that of the NC load can be, respectively, calculated as

$$|S_{\mathrm{sli}}| = \frac{|V_{\mathrm{s\_Ref}}|\left(|V_{\mathrm{s\_Ref}}| - \overrightarrow{V_{\mathrm{esri}}}\right)}{|Z_{\mathrm{oi}}|} \tag{6}$$

and

$$|S_{\mathrm{oi}}| = \frac{\left(|V_{\mathrm{s\_Ref}}| - \overrightarrow{V_{\mathrm{esri}}}\right)^2}{|Z_{\mathrm{oi}}|} \tag{7}$$

where $\overrightarrow{V_{\mathrm{esri}}}$ is the magnitude of the radial ES voltage on phase i with the polarity indicating that it is either in phase (positive) or in antiphase (negative) with the NC load voltage. The magnitude of the radial ES voltage on phase i can be calculated by using (5) and (6) as

$$|V_{\mathrm{esri}}| = |V_{\mathrm{s\_Ref}}| - \frac{|Z_{\mathrm{oi}}|\sqrt{(P_{\mathrm{s\_bal}} - P_{\mathrm{bi}})^2 + (Q_{\mathrm{s\_bal}} - Q_{\mathrm{bi}})^2}}{|V_{\mathrm{s\_Ref}}|} \tag{8}$$

The active power of the NC load on phase i can be found from (5), (7), and (8) as

$$\begin{aligned} P_{\mathrm{oi}} &= \frac{\left(|V_{\mathrm{s\_Ref}}| - \overrightarrow{V_{\mathrm{esri}}}\right)^2}{|Z_{\mathrm{oi}}|}\cos\phi_{\mathrm{oi}} \\ &= \frac{\left[(P_{\mathrm{s\_bal}} - P_{\mathrm{bi}})^2 + (Q_{\mathrm{s\_bal}} - Q_{\mathrm{bi}})^2\right]|Z_{\mathrm{oi}}|\cos\phi_{\mathrm{oi}}}{|V_{\mathrm{s\_Ref}}|^2} \end{aligned} \tag{9}$$

where ϕ_{oi} is the power angle of the NC load on phase i. Using (9), the ES active power on phase i can be calculated as

$$\begin{aligned} P_{\mathrm{esi}} &= P_{\mathrm{sli}} - P_{\mathrm{oi}} \\ &= P_{\mathrm{s\_bal}} - P_{\mathrm{bi}} - P_{\mathrm{oi}} \\ &= P_{\mathrm{s\_bal}} - P_{\mathrm{bi}} - \\ &\quad \frac{\left[(P_{\mathrm{s\_bal}} - P_{\mathrm{bi}})^2 + (Q_{\mathrm{s\_bal}} - Q_{\mathrm{bi}})^2\right]|Z_{\mathrm{oi}}|\cos\phi_{\mathrm{oi}}}{|V_{\mathrm{s\_Ref}}|^2}. \end{aligned} \tag{10}$$

Since the active and reactive branch power (P_{bi} and Q_{bi}), the supply-side reference voltage $|V_{\mathrm{s\_Ref}}|$, the impedance of the NC load $|Z_{\mathrm{oi}}|$, and the power angle of the NC load ϕ_{oi} are all constant in the steady state, only the balanced per-phase active and reactive power of the building ($P_{\mathrm{s\_bal}}$ and $Q_{\mathrm{s\_bal}}$) are considered as variables in (10). The three-phase ES active power is the sum of the ES active power on each phase. According to (10), this can be expressed as

$$\begin{aligned} P_{\mathrm{es}} &= P_{\mathrm{esa}} + P_{\mathrm{esb}} + P_{\mathrm{esc}} \\ &= K_1\,{P_{\mathrm{s\_bal}}}^2 + K_3\,{Q_{\mathrm{s\_bal}}}^2 + K_2\,P_{\mathrm{s\_bal}} + K_4\,Q_{\mathrm{s\_bal}} + K_5 \end{aligned} \tag{11}$$

where K_1, K_2, K_3, K_4, and K_5 are as indicated in (12), shown at the bottom of the next page.

Note that a positive quantity of $P_{\rm es}$ means that an active power flows from the power system to the ES and vice versa. Equation (11) indicates that $P_{\rm es}$ is a circular paraboloid function (as $K_1 = K_3$) of $P_{\rm s\_bal}$ and $Q_{\rm s\_bal}$ in 3-D $P_{\rm s\_bal}$–$Q_{\rm s\_bal}$–$P_{\rm es}$ space. The three-phase power system in Fig. 3 is symmetrically power balanced if the system operates at any point on the surface of this circular paraboloid. Also, a desired active power injection from (or absorption by) the ES can be chosen under a specified active and reactive power operation of the system ($P_{\rm s\_bal}$, $Q_{\rm s\_bal}$). By applying a first-order partial differentiation on $P_{\rm es}$ in (11) with respect to the specified power, we have

$$\frac{\partial P_{\rm es}}{\partial P_{\rm s\_bal}} = 2\,K_1\,P_{\rm s\_bal} + K_2 \tag{13}$$

and

$$\frac{\partial P_{\rm es}}{\partial Q_{\rm s\_bal}} = 2\,K_3\,Q_{\rm s\_bal} + K_4. \tag{14}$$

Hence, there exists a unique stationary point on the circular paraboloid function located at $(P_{\rm s\_bal}, Q_{\rm s\_bal}) = (-K_2/2K_1, -K_4/2K_3)$. Application of the second-order partial differentiation on $P_{\rm es}$ gives

$$\frac{\partial^2 P_{\rm es}}{\partial {P_{\rm s\_bal}}^2} = \begin{cases} 2K_1 < 0, \text{ for } (R_{\rm oa} + R_{\rm ob} + R_{\rm oc}) > 0 \\ 2K_1 > 0, \text{ for } (R_{\rm oa} + R_{\rm ob} + R_{\rm oc}) < 0 \end{cases} \tag{15}$$

$$\frac{\partial^2 P_{\rm es}}{\partial {Q_{\rm s\_bal}}^2} = \begin{cases} 2K_3 < 0, \text{ for } (R_{\rm oa} + R_{\rm ob} + R_{\rm oc}) > 0 \\ 2K_3 > 0, \text{ for } (R_{\rm oa} + R_{\rm ob} + R_{\rm oc}) < 0 \end{cases} \tag{16}$$

and

$$\frac{\partial^2 P_{\rm es}}{\partial P_{\rm s\_bal} \partial Q_{\rm s\_bal}} = 0. \tag{17}$$

Equations (15)–(17) are used for classifying the stationary point of the function $P_{\rm es}$ in (11). The determinant $\det(P_{\rm s\_bal}, Q_{\rm s\_bal})$ of the Hessian matrix of the function $P_{\rm es}$, $\mathbf{H}(P_{\rm s\_bal}, Q_{\rm s\_bal})$, is

$$\begin{aligned} \det(P_{\rm s\_bal}, Q_{\rm s\_bal}) &= \det(\mathbf{H}(P_{\rm s\_bal}, Q_{\rm s\_bal})) \\ &= \det \begin{bmatrix} \dfrac{\partial^2 P_{\rm es}}{\partial {P_{\rm s\_bal}}^2} & \dfrac{\partial^2 P_{\rm es}}{\partial P_{\rm s\_bal} \partial Q_{\rm s\_bal}} \\ \dfrac{\partial^2 P_{\rm es}}{\partial P_{\rm s\_bal} \partial Q_{\rm s\_bal}} & \dfrac{\partial^2 P_{\rm es}}{\partial {Q_{\rm s\_bal}}^2} \end{bmatrix} \\ &= \frac{\partial^2 P_{\rm es}}{\partial {P_{\rm s\_bal}}^2} \cdot \frac{\partial^2 P_{\rm es}}{\partial {Q_{\rm s\_bal}}^2} - \left(\frac{\partial^2 P_{\rm es}}{\partial P_{\rm s\_bal} \partial Q_{\rm s\_bal}} \right)^2 \end{aligned} \tag{18}$$

where det is the denotation for determinant. According to the second-partial-derivative test for two variables [27], since $\det(P_{\rm s\_bal}, Q_{\rm s\_bal})$ is always positive [referring to the results in (15)–(18)], the stationary point $(P_{\rm s\_bal}, Q_{\rm s\_bal}) = (-K_2/2K_1, -K_4/2K_3)$ must be a unique extremum of the function $P_{\rm es}$. This extremum is the maximum point and the circular paraboloid is concave downward when $\partial^2 P_{\rm es}/\partial {P_{\rm s\_bal}}^2 < 0$. This is the case where the constant $K_1 < 0$ as indicated in (15). On the other hand, the extremum is the minimum point and the circular paraboloid is concave upward when $\partial^2 P_{\rm es}/\partial {P_{\rm s\_bal}}^2 > 0$ ($K_1 > 0$). It is concluded that the concavity of the circular paraboloid function (determined by the constant K_1) depends on the summed value of the resistive part of the NC load on each phase as described by (15).

To show the properties of the circular paraboloid function, six cases of the NC load power and the branch power in per-unit (p.u.) representation are included as shown in Table I. The magnitude of the supply voltage ($V_{\rm si}$) and the average per-phase nominal active power of the system ($P_{\rm nom\_s}/3$) are chosen to be 1 p.u. Fig. 4(a)–(c) shows the phasor diagram of the NC load impedance in cases A, B, and C, respectively, where their NC loads are, respectively, balanced positive pure resistive, balanced positive-resistive inductive, and unbalanced pure resistive. Their corresponding circular paraboloid functions are plotted in Fig. 5(a)–(c), respectively. The constant K_1 in all the three cases is negative and these circular paraboloid functions are all concave downward. On the other hand, Fig. 4(d)–(f)

$$\begin{aligned} K_1 &= -\frac{|Z_{\rm oa}|\cos(\phi_{\rm oa})}{|V_{\rm s\_Ref}|^2} - \frac{|Z_{\rm ob}|\cos(\phi_{\rm ob})}{|V_{\rm s\_Ref}|^2} - \frac{|Z_{\rm oc}|\cos(\phi_{\rm oc})}{|V_{\rm s\_Ref}|^2} \\ K_2 &= 3 + 2\frac{P_{\rm ba}\,|Z_{\rm oa}|\cos(\phi_{\rm oa})}{|V_{\rm s\_Ref}|^2} + 2\frac{P_{\rm bb}\,|Z_{\rm ob}|\cos(\phi_{\rm ob})}{|V_{\rm s\_Ref}|^2} + 2\frac{P_{\rm bc}\,|Z_{\rm oc}|\cos(\phi_{\rm oc})}{|V_{\rm s\_Ref}|^2} \\ K_3 &= -\frac{|Z_{\rm oa}|\cos(\phi_{\rm oa})}{|V_{\rm s\_Ref}|^2} - \frac{|Z_{\rm ob}|\cos(\phi_{\rm ob})}{|V_{\rm s\_Ref}|^2} - \frac{|Z_{\rm oc}|\cos(\phi_{\rm oc})}{|V_{\rm s\_Ref}|^2} \\ K_4 &= 2\frac{Q_{\rm ba}\,|Z_{\rm oa}|\cos(\phi_{\rm oa})}{|V_{\rm s\_Ref}|^2} + 2\frac{Q_{\rm bb}\,|Z_{\rm ob}|\cos(\phi_{\rm ob})}{|V_{\rm s\_Ref}|^2} + 2\frac{Q_{\rm bc}\,|Z_{\rm oc}|\cos(\phi_{\rm oc})}{|V_{\rm s\_Ref}|^2} \\ K_5 &= -P_{\rm ba} - \frac{\left({P_{\rm ba}}^2 + {Q_{\rm ba}}^2\right)|Z_{\rm oa}|\cos(\phi_{\rm oa})}{|V_{\rm s\_Ref}|^2} - P_{\rm bb} - \frac{\left({P_{\rm bb}}^2 + {Q_{\rm bb}}^2\right)|Z_{\rm ob}|\cos(\phi_{\rm ob})}{|V_{\rm s\_Ref}|^2} - P_{\rm bc} - \frac{\left({P_{\rm bc}}^2 + {Q_{\rm bc}}^2\right)|Z_{\rm oc}|\cos(\phi_{\rm oc})}{|V_{\rm s\_Ref}|^2} \end{aligned} \tag{12}$$

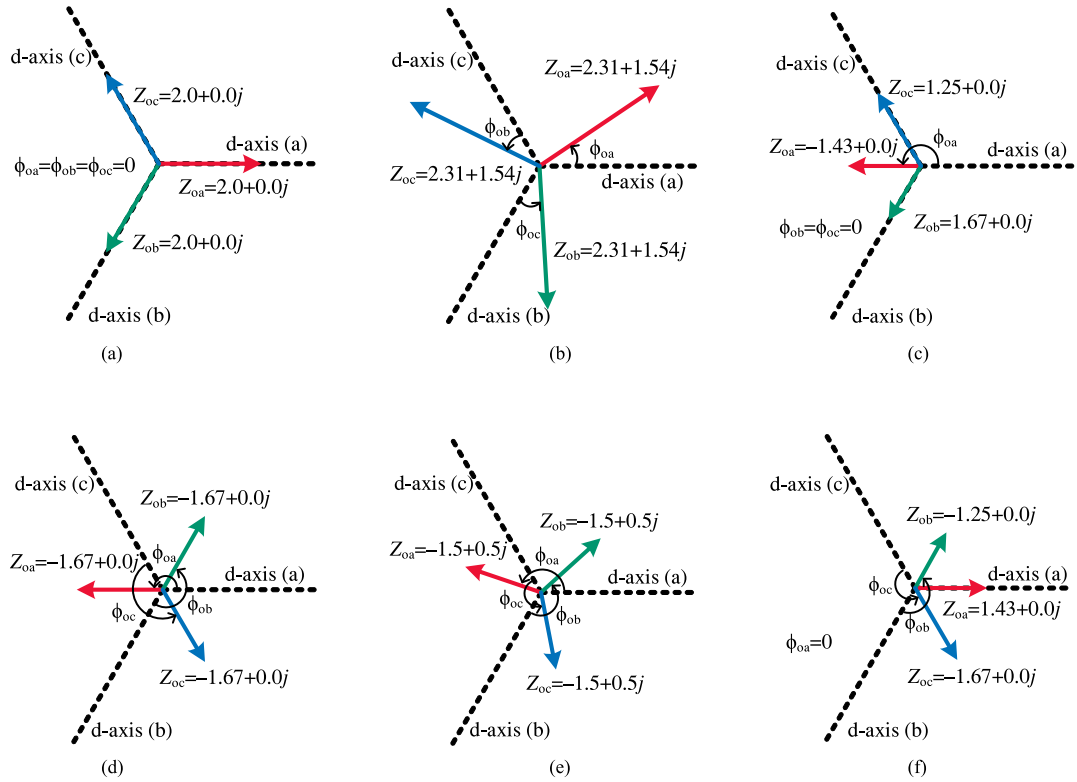

Fig. 4. Six cases of NC loads with respect to the corresponding nominal complex power indicated in Table I. (Per-unit representation.) (a) Case A: A pure positive-resistive NC load. (b) Case B: A positive-resistive-inductive NC load. (c) Case C: An unbalanced NC load with the three-phase sum of positive resistive value. (d) Case D: A pure negative-resistive NC load. (e) Case E: A negative-resistive-capacitive NC load. (f) Case F: An unbalanced NC load with the three-phase sum of negative resistive value.

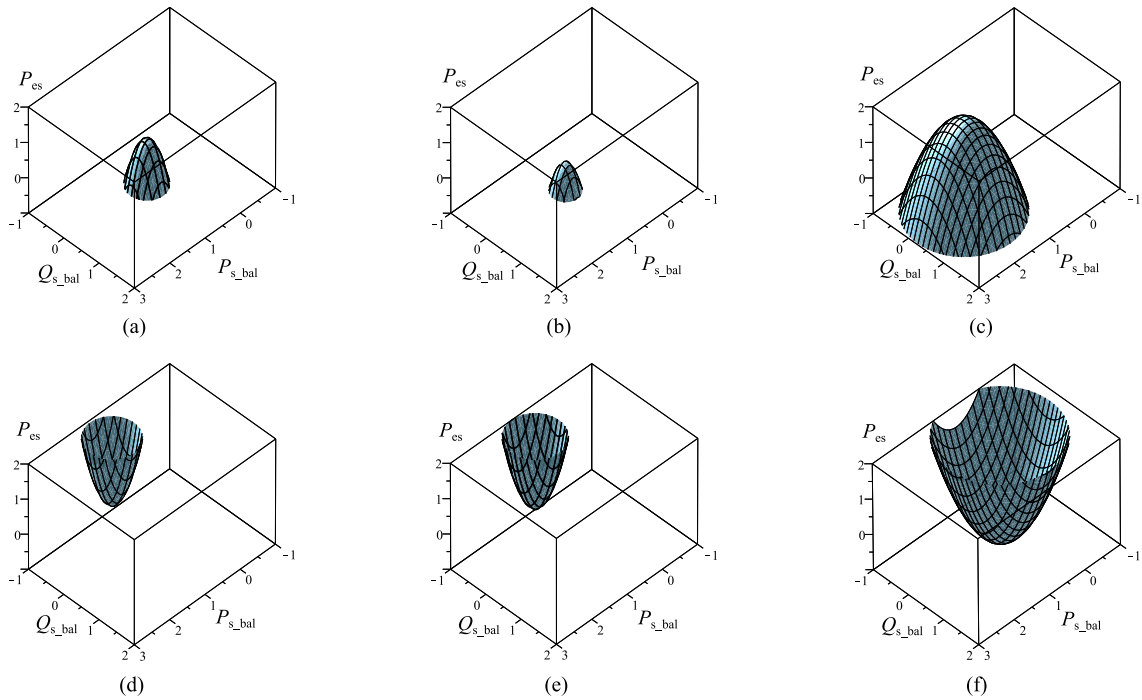

Fig. 5. Six cases of the circular paraboloid function in (11) with respect to the corresponding parameters in Table I. (Per-unit representation.) (a) Case A: A pure positive-resistive NC load. ($K_1 = -6, K_2 = 9, K_3 = -6, K_4 = 1.2, K_5 = -3.14$). (b) Case B: A positive-resistive-inductive NC load. ($K_1 = -6, K_2 = 12.69, K_3 = -6.92, K_4 = 2.31, K_5 = -6.21$). (c) Case C: An unbalanced NC load with the three-phase sum of positive resistive value. ($K_1 = -1.49, K_2 = 4.96, K_3 = -1.49, K_4 = 0.71, K_5 = -2.68$). (d) Case D: A pure negative-resistive-capacitive NC load. ($K_1 = 5, K_2 = -13, K_3 = 5, K_4 = 3.33, K_5 = 9.1$). (e) Case E: A negative-resistive-capacitive NC load. ($K_1 = 4.5, K_2 = -11.4, K_3 = 4.5, K_4 = 3, K_5 = 7.71$). (f) Case F: An unbalanced NC load with the three-phase sum of negative resistive value. ($K_1 = 1.49, K_2 = -1.89, K_3 = 1.49, K_4 = -0.71, K_5 = -0.23$).

TABLE I
PARAMETERS OF THE SYSTEM IN EXAMPLES

Case	Variable	Phase *a* (p.u.)	Phase *b* (p.u.)	Phase *c* (p.u.)
/	$\lvert V_{\rm si}\rvert$	1	1	1
/	$P_{\rm s\_bal}$	1	1	1
A	$P_{\rm oi}+Q_{\rm oi}$	$0.5+j0.0$	$0.5+j0.0$	$0.5+j0.0$
	$P_{\rm bi}+Q_{\rm bi}$	$0.6+j0.2$	$0.5+j0.1$	$0.4+j0.0$
B	$P_{\rm oi}+Q_{\rm oi}$	$0.3+j0.2$	$0.3+j0.2$	$0.3+j0.2$
	$P_{\rm bi}+Q_{\rm bi}$	$0.7+j0.3$	$1.0+j0.2$	$0.4+j0.0$
C	$P_{\rm oi}+Q_{\rm oi}$	$-0.7+j0.0$	$0.8+j0.0$	$0.6+j0.0$
	$P_{\rm bi}+Q_{\rm bi}$	$0.8-j0.6$	$0.9-j0.4$	$0.6-j0.0$
D	$P_{\rm oi}+Q_{\rm oi}$	$-0.6+j0.0$	$-0.6+j0.0$	$-0.6+j0.0$
	$P_{\rm bi}+Q_{\rm bi}$	$1.7-j0.6$	$1.8-j0.4$	$1.3+j0.0$
E	$P_{\rm oi}+Q_{\rm oi}$	$-0.6-j0.2$	$-0.6-j0.2$	$-0.6-j0.2$
	$P_{\rm bi}+Q_{\rm bi}$	$1.7-j0.6$	$1.8-j0.4$	$1.3+j0.0$
F	$P_{\rm oi}+Q_{\rm oi}$	$0.7+j0.0$	$-0.8+j0.0$	$-0.6+j0.0$
	$P_{\rm bi}+Q_{\rm bi}$	$1.0-j0.6$	$1.5-j0.4$	$1.2+j0.0$

shows the phasor diagram of the NC load impedance in cases D, E, and F, respectively, where their NC loads are, respectively, balanced negative pure resistive, balanced negative-resistive capacitive, and unbalanced pure resistive. Their corresponding circular paraboloid functions are plotted in Fig. 5(d)–(f), respectively. For all the three cases, the constant K_1 is positive and the circular paraboloid functions are all concave upward.

Equation (11) can be used to determine the corresponding value of the ES voltage on each phase. Given a specific desired balanced active and reactive power operating point of the system ($P_{\rm s\_bal}$, $Q_{\rm s\_bal}$), the corresponding radial ($V_{\rm esri}$) and chordal ES voltage ($V_{\rm esci}$) on phase i can be calculated as

$$|V_{\rm esri}| = |V_{\rm s\_Ref}| - \frac{|Z_{\rm oi}|\sqrt{(P_{\rm s\_bal}-P_{\rm bi})^2+(Q_{\rm s\_bal}-Q_{\rm bi})^2}}{|V_{\rm s\_Ref}|} \tag{19}$$

$$\begin{aligned}\theta_{\rm esri} &= \theta_{\rm oi}\\ &= \phi_{\rm oi}-\phi_{\rm sli}\\ &= \phi_{\rm oi}-\arg\left[(P_{\rm s\_bal}-P_{\rm bi})+j\,(Q_{\rm s\_bal}-Q_{\rm bi})\right]\end{aligned} \tag{20}$$

$$|V_{\rm esci}| = \sqrt{2|V_{\rm s\_Ref}|^2\,(1-\cos(\theta_{\rm oi}))} \tag{21}$$

$$\theta_{\rm esci} = -{\rm sgn}(\theta_{\rm oi})\frac{\pi-|\theta_{\rm oi}|}{2} \tag{22}$$

where $\theta_{\rm esri}$, $\theta_{\rm oi}$, $\theta_{\rm esci}$ are, respectively, the phasor angle of the radial ES voltage, NC load voltage, and chordal ES voltage with respect to their corresponding grid voltage ($V_{\rm si}$) on phase i. The notations $\arg(.)$ and ${\rm sgn}(.)$ are defined as the argument of the complex number and the signum function, respectively. Equations (19) and (20) are for the radial ES voltages, while (21) and (22) are for the chordal ones. The derivations of (19)–(22) and their explanations can be found in [26].

III. OPTIMUM OPERATING CONDITIONS FOR RESTORING POWER BALANCE

The circular paraboloid function given in (11) can be used to 1) determine the three-phase power-balanced operating point of a power system regulated by the ES and 2) optimize the active power usage in the ES such that the battery storage capacity can be minimized. The following two conditions are possible with the system shown in Fig. 3.

1) The power balance can be restored by the ES with active power injection into the system. While there are multiple solutions, there exists a solution that requires minimum active power from the ES.
2) The power balance can be restored by the ES without active power injection into the system. While there are multiple solutions, there exists an optimum solution that involves the minimum deviation from the original average active power value of the three-phase system ($P_{\rm nom\_s}$).

These two cases are separately discussed in this section. The minimum use of active power would lead to the minimization of the energy storage capacity in the ES.

The ES under consideration is a bidirectional dc–ac power converter with a battery storage connected to its dc bus. The active power delivered from the battery storage (denoted as $P_{\rm es\_dc}$) is equal to the sum of the power loss in the bidirectional converter (denoted as $P_{\rm es\_loss}$) and the ES active power injected to the grid (i.e., $P_{\rm es\_dc}=P_{\rm es\_loss}+P_{\rm es}$). If the power loss of this bidirectional converter is neglected ($P_{\rm es\_loss}=0\,{\rm W}$) and the ES does not deliver active power to the grid ($P_{\rm es}=0\,{\rm W}$), there is no requirement for energy storage in the ES ($P_{\rm es\_dc}=0\,{\rm W}$). Under this premise, the operating point of the system should lie on the locus defined by the intersection of the circular paraboloid function and the plane $P_{\rm es}=0$ p.u. This locus is

$$K_1\,{P_{\rm s\_bal}}^2+K_3\,{Q_{\rm s\_bal}}^2+K_2\,P_{\rm s\_bal}+K_4\,Q_{\rm s\_bal}+K_5=0. \tag{23}$$

A. Restoring Power Balance With Minimum Active Power by the ES

In the case that (23) does not give a real solution, it means that there is no intersection between the circular paraboloid function and the plane $P_{\rm es}=0$ p.u. In this case, $P_{\rm es}$ cannot reach zero and a minimized value of $|P_{\rm es}|$ should be determined. Equation (23) can be rewritten as

$$\begin{aligned}&\left(P_{\rm s\_bal}+\frac{K_2}{2K_1}\right)^2+\left(Q_{\rm s\_bal}+\frac{K_4}{2K_1}\right)^2\\ &\quad=\left(\frac{K_2}{2K_1}\right)^2+\left(\frac{K_4}{2K_1}\right)^2-\frac{K_5}{K_1}.\end{aligned} \tag{24}$$

This is the equation of a circle on the $P_{\rm s\_bal}$–$Q_{\rm s\_bal}$ plane with the origin located at $(-K_2/2K_1, -K_4/2K_3)$ and its radius equals to the square root of the right-hand side of the equation. The condition for this circle to be imaginary is that the radius must be smaller than zero, which gives

$${K_2}^2+{K_4}^2<4K_5K_1. \tag{25}$$

Hence, a minimum value of $|P_{\rm es}|$ exists and it is located at $(P_{\rm s\_bal}, Q_{\rm s\_bal})=(-K_2/2K_1, -K_4/2K_3)$ (which is the vertex and the extremum of the circular paraboloid function) if and only if (25) holds. Fig. 5(a) and (d) is redrawn with the plane of $P_{\rm es}=0$ p.u. They are shown in Fig. 6(a) and (b), respectively.

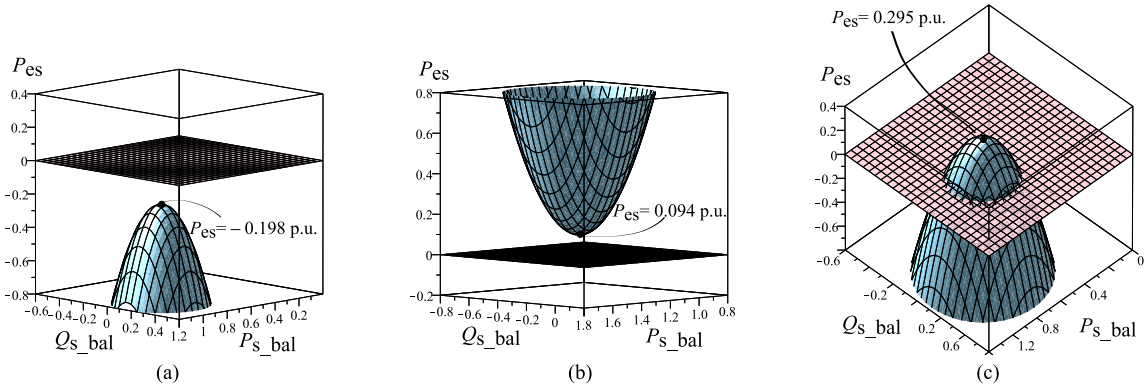

Fig. 6. Three examples show different scenarios in the circular paraboloid function interacting with the plane $P_{\rm es} = 0$. (Per-unit representation.) (a) The circular paraboloid is plotted using (11) with the data in case B. (b) The circular paraboloid is plotted using (11) with the data in case D. (c) The circular paraboloid is plotted using (11) with the data in case A.

In Fig. 6(a), the circular paraboloid function in case B is concave downward with the maximum value of $P_{\rm es} = -0.198$ p.u. at the vertex. Any operating point on the surface of the circular paraboloid is a solution for the ES to restore power balance. The vertex is, therefore, the optimum solution because it has the shortest distance to the plane of $P_{\rm es} = 0$ p.u. Operating at the vertex point means in this case that power balance can be restored with the battery of the ES being discharged to provide the minimum amount of active power.

On the other hand, Fig. 6(b) shows the condition for case D. The circular paraboloid function is concave upward and the minimum amount of active power absorbed by the ES is $P_{\rm es} = 0.094$ p.u. Operating at this vertex is the optimum solution because the battery of the ES will be charged to absorb the minimum active power in order to restore the power balance.

B. Restoring Power Balance Without Active Power from the ES

The ES does not need to inject active power into the system if (23) exists real solutions. In this case, the plane $P_{\rm es} = 0$ p.u. intersects with the surface of the paraboloid as shown in an example of Fig. 6(c). Unlike the condition in Section III-A of which an optimum operating point of the system is unique (at the vertex of the circular paraboloid function), the system discussed in this section can operate at any intersection point lying on the circle in (23). In order to visualize the characteristics of the circular paraboloid function and quantitatively identify the locus of ($P_{\rm s\_bal}$, $Q_{\rm s\_bal}$), the data in case A as shown in Table I are used as an example. Substituting the parameters of case A in Table I into (11) gives

$$P_{\rm es} = -6{P_{\rm s\_bal}}^2 + 9P_{\rm s\_bal} - 6{Q_{\rm s\_bal}}^2 + 1.2Q_{\rm s\_bal} - 3.14. \tag{26}$$

Fig. 6(c) shows the circular paraboloid function in (26) and the plane $P_{\rm es} = 0$ p.u. Since the NC load is positive resistive, the vertex of the circular paraboloid function is the maximum point of $P_{\rm es}$. This point is located at ($P_{\rm s\_bal}$, $Q_{\rm s\_bal}$, $P_{\rm es}$) = (0.75 p.u., 0.1 p.u., 0.295 p.u.), which can be obtained from (13), (14), and (26).

The operating locus of the system power ($P_{\rm s\_bal}$, $Q_{\rm s\_bal}$) that the ES operates in case A such that no active power is injected by the ES during the power-balanced condition is shown in Fig. 7.

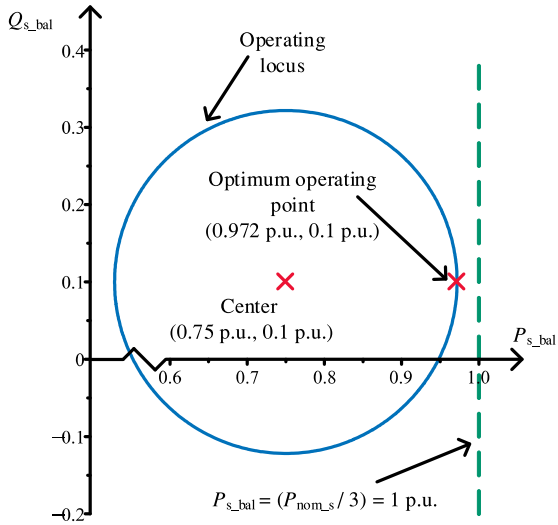

Fig. 7. Operating locus of the system power for the ES to regulate the system in case A to be power balanced without injecting active power from the ES.

Its equation is

$$-6{P_{\rm s\_bal}}^2 + 9P_{\rm s\_bal} - 6{Q_{\rm s\_bal}}^2 + 1.2Q_{\rm s\_bal} - 3.14 = 0. \tag{27}$$

This equation represents a circle obtained by considering the intersection of the circular paraboloid function and the plane $P_{\rm es} = 0$ p.u. as shown in Fig. 6(c). Next, the ES voltage $V_{\rm esi}$ on phase i can be obtained from (19)–(22). Since there is no explicit function to express the ES voltage, the locus of the ES voltage can be expressed in terms of $P_{\rm s\_bal}$ and $Q_{\rm s\_bal}$, which is indicated as

$$\begin{aligned} V_{\rm esi} &= V_{\rm esri} + V_{\rm esci} = |V_{\rm esri}|\angle\theta_{\rm esri} + |V_{\rm esci}|\angle\theta_{\rm esci} \\ &= \left[|V_{\rm s\_Ref}| - \frac{|Z_{\rm oi}|\sqrt{\left(P_{\rm s\_bal} - P_{\rm bi}\right)^2 + \left(Q_{\rm s\_bal} - Q_{\rm bi}\right)^2}}{|V_{\rm s\_Ref}|}\right] \\ &\quad \angle\left\{\phi_{\rm oi} - \arg\left[\left(P_{\rm s\_bal} - P_{\rm bi}\right) + j\left(Q_{\rm s\_bal} - Q_{\rm bi}\right)\right]\right\} + \\ &\quad \left[\sqrt{2|V_{\rm s\_Ref}|^2\left(1 - \cos\left(\theta_{\rm oi}\right)\right)}\right] \angle\left[-{\rm sgn}(\theta_{\rm oi})\frac{\pi - |\theta_{\rm oi}|}{2}\right]. \end{aligned} \tag{28}$$

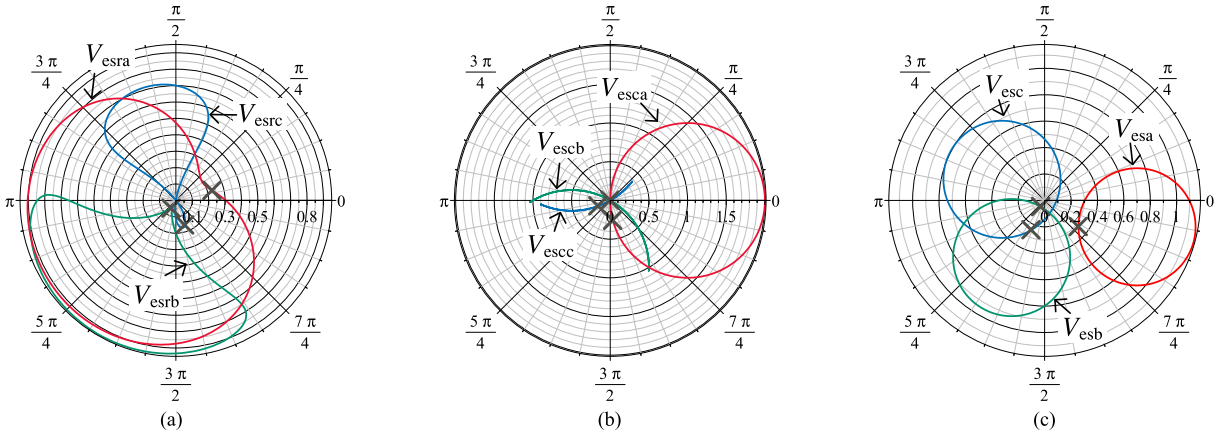

Fig. 8. Loci of (a) radial ES voltages, (b) chordal ES voltages, and (c) resultant ES voltages in case A. (Phase *a*: red, phase *b*: green, phase *c*: blue.) (The polar angles on each phase are: phase *a*: $\theta_{\rm esa}$, phase *b*: $(\theta_{\rm esb} - 2\pi/3)$, and phase *c*: $(\theta_{\rm esc} + 2\pi/3)$.) (The cross markers are the optimum operating points.)

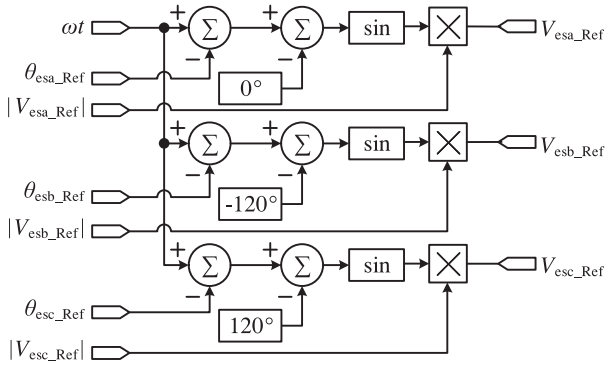

Fig. 9. Control circuit of the ES adopted in the PSIM simulation in Section IV.

Hence, the locus of the ES voltage can be obtained by substituting the implicit function (27) into (28). Fig. 8(a)–(c) shows the loci of the radial ES voltage, the chordal ES voltage, and the resultant ES voltage (vector sum of $V_{\rm esri}$ and $V_{\rm esci}$) of each phase, respectively.

It is important to find the optimum operating point of the system within these loci. One possible optimum point of the system is that the balanced per-phase active power of the system $P_{\rm s\_bal}$ should be as close as possible to the average per-phase nominal active power that $(P_{\rm nom\_s}/3)$ (which is highlighted in a dotted line in Fig. 7).[1] As a result, the optimization criterion is to minimize the difference between $P_{\rm s\_bal}$ and $P_{\rm nom\_s}/3$. This minimized difference, in geometry sense, is equivalent to the shortest distance between a point on the line $P_{\rm s\_bal} = 1$ p.u. and a point on the circle [in (27)], as shown in Fig. 7. Consequently, the optimum operating point is located at where the value of $|P_{\rm s\_bal}|$ is maximum. By applying a first-order partial differentiation on (23) with respect to $Q_{\rm s\_bal}$, we have

$$Q_{\rm s\_bal} = -\frac{K_4}{2K_3}. \tag{29}$$

By substituting (29) into (23), the optimum point of $P_{\rm s\_bal}$ can be derived as

$$P_{\rm s\_bal} = \begin{cases} \dfrac{-K_2K_3 + \sqrt{-4K_1{K_3}^2K_5 + K_1K_3{K_4}^2 + {K_2}^2{K_3}^2}}{2K_1K_3} \\ \qquad (\text{for } P_{\rm s\_nom} > 0) \\ \dfrac{-K_2K_3 - \sqrt{-4K_1{K_3}^2K_5 + K_1K_3{K_4}^2 + {K_2}^2{K_3}^2}}{2K_1K_3} \\ \qquad (\text{for } P_{\rm s\_nom} < 0) \end{cases}. \tag{30}$$

From (29) and (30), the optimum point of the system is calculated for case A as $(P_{\rm s\_bal}, Q_{\rm s\_bal}) = (0.972\ \text{p.u.}, 0.1\ \text{p.u.})$. The corresponding ES voltage on each phase is calculated, using (28), as $V_{\rm esa} = 0.325\angle -0.66\,\text{p.u.}$, $V_{\rm esb} = 0.057\angle 0\ \text{p.u.}$, and $V_{\rm esc} = 0.246\angle 2.19\,\text{p.u.}$ This optimum operating point of the ES voltage is marked on Fig. 8(a)–(c).

IV. Simulation and Experimental Results

In the first part, a simulation is conducted to validate the proposed method for the restoration of power balance in a three-phase unbalanced power system. In the second part, the ability of the proposed method for the optimization of active power usage in the ES is verified with simulation. The experimental validation is discussed in the third part.

A. Restoration of Power Balance

The validation on the proposed RCD method for the restoration of power balance in a three-phase unbalanced power system is conducted using the simulation software PSIM version 10.0. The system schematic adopted in the simulation is shown in Fig. 10, where three controlled voltage sources are adopted to

[1]It should be noted that for illustration purpose, only one optimum operating point that is closest to the average per-phase active power of the system is chosen and presented in the analysis. There are other possible optimum operating points in regard to the parameters being optimized. For example, another possible optimum operating point can be found when the reactive power of the system is regarded as zero (or minimum) to maximize the power factor of the system.

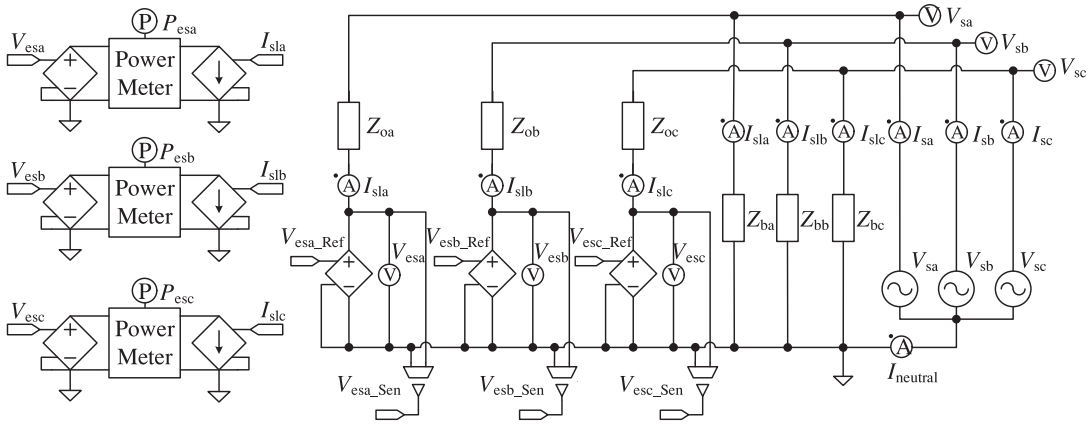

Fig. 10. Power stage of the ES adopted in the PSIM simulation in Section IV.

model the three-phase ES. Both case B and case F shown in Table I are adopted in the simulation.

The magnitude of the phase-to-neutral grid voltage and the average per-phase nominal active power of the system are chosen as $|V_{\rm si}| = 220$ V (1 p.u.) and $P_{\rm nom\_s}/3 = 1$ kW (1 p.u.) in the simulation, respectively. The ES voltage is precalculated by the proposed algorithm discussed in Sections II and III. The calculated magnitude ($|V_{\rm esa\_Ref}|$, $|V_{\rm esb\_Ref}|$ and $|V_{\rm esc\_Ref}|$) and phases ($\theta_{\rm esa\_Ref}$, $\theta_{\rm esb\_Ref}$ and $\theta_{\rm esc\_Ref}$) of the ES voltage references are used as the controlled signals of these three controlled voltage sources as shown in Fig. 9.

The simulation is first conducted using the values of the NC load and the branch load in case B in Table I. Fig. 11(a) shows the steady-state waveforms of the neutral and line currents before the activation of the ES. They are found as $|I_{\rm sa}|\angle\theta_{\rm sa} = 5.082\angle -\ 0.464$ A, $|I_{\rm sb}|\angle\theta_{\rm sb} = 6.182\angle -0.298$ A, and $|I_{\rm sc}|\angle\theta_{\rm sc} = 3.308\angle -0.278$ A, and their phasor diagrams are shown in Fig. 11(b). The three-phase line currents are transformed into their symmetrical components using

$$\begin{bmatrix} |I_{\rm szero}|\angle\theta_{\rm szero} \\ |I_{\rm spos}|\angle\theta_{\rm spos} \\ |I_{\rm sneg}|\angle\theta_{\rm sneg} \end{bmatrix} = \begin{bmatrix} 1 & 1 & 1 \\ 1 & a & a^2 \\ 1 & a^2 & a \end{bmatrix} \begin{bmatrix} |I_{\rm sa}|\angle\theta_{\rm sa} \\ |I_{\rm sb}|\angle\theta_{\rm sb} \\ |I_{\rm sc}|\angle\theta_{\rm sc} \end{bmatrix} \tag{31}$$

where a is defined as $\cos(2\pi/3) + j\sin(2\pi/3)$, and $|I_{\rm szero}|\angle\theta_{\rm szero}$, $|I_{\rm spos}|\angle\theta_{\rm spos}$, and $|I_{\rm sneg}|\angle\theta_{\rm sneg}$ are, respectively, the zero-sequence, positive-sequence, and negative-sequence component of the current. The phasor diagram of the symmetrical components is shown in Fig. 11(c). The objective of this transformation is to obtain the symmetrical-component values for indicating the degree of balance of the system.

Next, the simulation is repeated with the ES voltages calculated based on the proposed RCD method. Since the solution of (23) is imaginary, the optimum operating point of the system can be found from (13) and (14) as $P_{\rm s\_bal} = 917$ W and $Q_{\rm s\_bal} = 167$ VAr. Substituting these values into (28) gives the ES voltage on each phase. They are $|V_{\rm esa}|\angle\theta_{\rm esa} = 209.65\angle -0.738$ V, $|V_{\rm esb}|\angle\theta_{\rm esb} = 273.82\angle 0.0412$ V, and $|V_{\rm esc}|\angle\theta_{\rm esc} = 133.76\angle -2.401$ V. The corresponding waveforms of the ES voltage in each power phase are shown in Fig. 15(a). The simulated line currents are $|I_{\rm sa}|\angle\theta_{\rm sa} = |I_{\rm sb}|\angle\theta_{\rm sb} = |I_{\rm sc}|\angle\theta_{\rm sc} = 4.235\angle -\ 0.180$ A. Fig. 12(a)–(c), respectively, show the simulated line-current waveforms, their phasor diagrams and their symmetrical components. According to Figs. 11(c) and 12(c), the proposed RCD control method can control the ES to mitigate both the zero-sequence and negative-sequence currents to zero.

The simulation is then repeated with the values of the NC load and the branch load given in case F. In the proposed RCD method, the operating point of the system is calculated following the analysis presented in Section III-B, which gives $P_{\rm s\_bal} = 1421$ W, $Q_{\rm s\_bal} = 240$ VAr, $|V_{\rm esa}|\angle\theta_{\rm esa} = 278.14\angle 1.251$ V, $|V_{\rm esb}|\angle\theta_{\rm esb} = 265.21\angle -0.726$ V, and $|V_{\rm esc}|\angle\theta_{\rm esc} = 313.78\angle -0.284$ V. The simulation waveforms of the line currents, their phasor diagrams and their symmetrical components without the activation of the ES are shown in Fig. 13(a)–(c), respectively. The simulation waveforms of line currents with the ES under the RCD control method are shown in Fig. 14(a)–(c). The corresponding waveforms of the ES voltage in each power phase are shown in Fig. 15(b). The results depicted in Figs. 13(c) and 14(c) indicate that the proposed RCD method can control the ES to mitigate both zero-sequence and negative-sequence currents to zero.

From the presented results, it can be concluded that the proposed RCD method can be applied to the ES with both negative (case F) and positive (case B) resistive NC load and this NC load can be either balanced (case B) or unbalanced (case F), and this method can mitigate both the zero-sequence and the negative-sequence currents to zero such that the system is symmetrically power balanced.

B. Optimization on the Active Power Usage in the ES

This section verifies the ability of the proposed method for the optimization on the active power usage in the ES. The same configuration used in the simulation in Section IV-A is adopted. Case B is used to demonstrate the procedures on determining the minimized ES active power as discussed in Section III-A. Case F is used to demonstrate how zero ES active power is required for power balancing as discussed in Section III-B. In

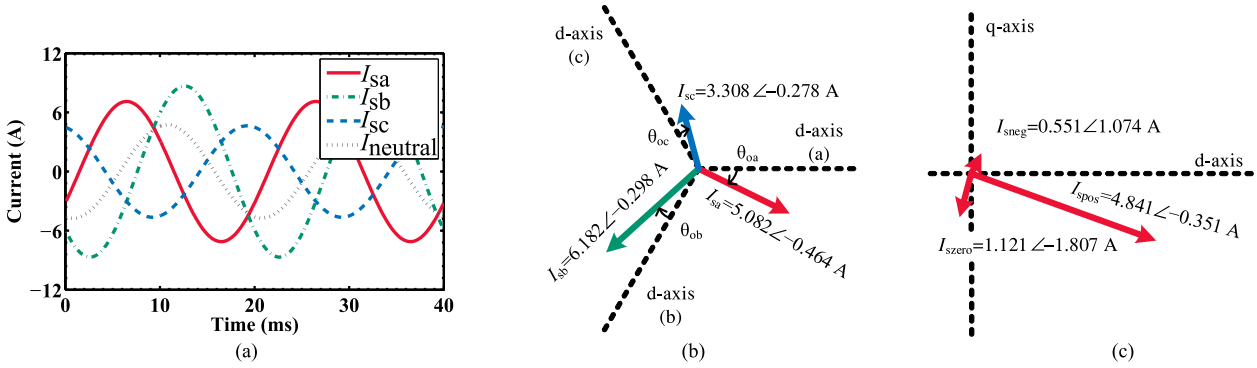

Fig. 11. Simulation results for case B with the ES deactivated. (a) Steady-state waveforms of the line currents and the neutral current without the activation of the ES. (b) Corresponding phasor diagram of the three-phase line currents in Fig. 11(a). (c) Corresponding phasor diagram of the symmetrical-component currents in Fig. 11(b).

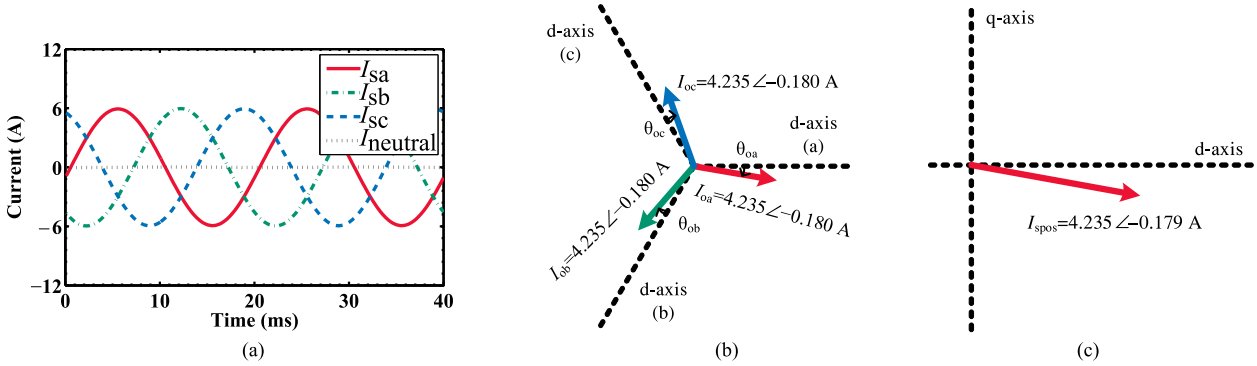

Fig. 12. Simulation results for case B with the ES under RCD control. (a) Steady-state waveforms of the line currents and the neutral current with the ES under the proposed RCD control. (b) Corresponding phasor diagram of the three-phase line current in Fig. 12(a). (c) Corresponding phasor diagram of the symmetrical-component currents in Fig. 12(b).

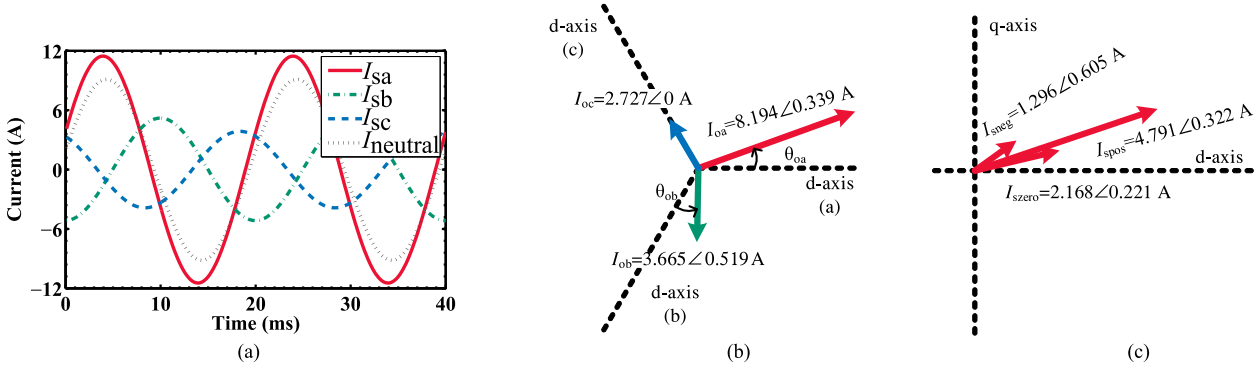

Fig. 13. Simulation results for case F with the ES deactivated. (a) Steady-state waveforms of the line currents and the neutralcurrent without the activation of the ES. (b) Corresponding phasor diagram of the three-phase line current in Fig. 13(a). (c) Corresponding phasor diagram of the symmetrical-component currents in Fig. 13(b).

case B, the vertex of the circular paraboloid function in (11), according to (13) and (14), is located at

$$\begin{aligned}(P_{\text{s\_bal}},\, Q_{\text{s\_bal}}) &= (-K_2/2K_1, -K_4/2K_3) \\ &= (917\ \text{W}, 167\ \text{VAr})\,.\end{aligned} \tag{32}$$

This is the optimum operating point, at which the ES delivers a minimum active power to the system in case B. Putting (32) and the data of case B in Table I into (11) gives

$$\begin{aligned}P_{\text{es}} &= P_{\text{esa}} + P_{\text{esb}} + P_{\text{esc}} \\ &= K_1 {P_{\text{s\_bal}}}^2 + K_3 {Q_{\text{s\_bal}}}^2 + K_2 P_{\text{s\_bal}} + K_4 Q_{\text{s\_bal}} + K_5 \\ &= -198.08\ \text{W}.\end{aligned} \tag{33}$$

Fig. 16(a) shows the simulated value of the ES active power on each phase and the sum of these powers

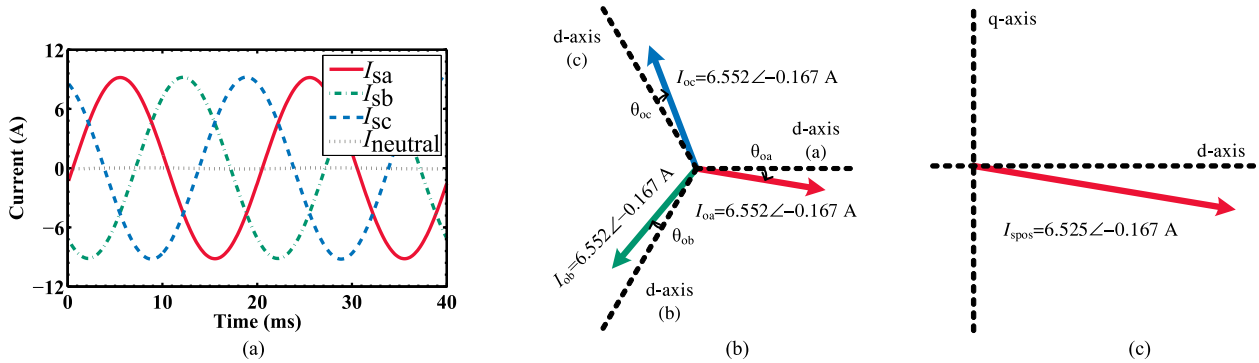

Fig. 14. Simulation results for case F with the ES under RCD control. (a) Steady-state waveforms of the line currents and the neutral current with the ES under the proposed RCD control. (b) Corresponding phasor diagram of the three-phase line current in Fig. 14(a). (c) Corresponding phasor diagram of the symmetrical-component currents in Fig. 14(b).

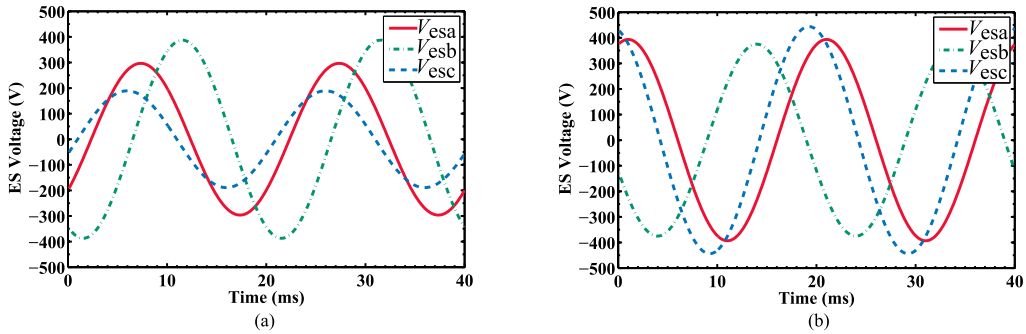

Fig. 15. Steady-state simulation waveforms of the ES voltage on each phase with the ES under the proposed RCD control. (a) Case B. (b) Case F.

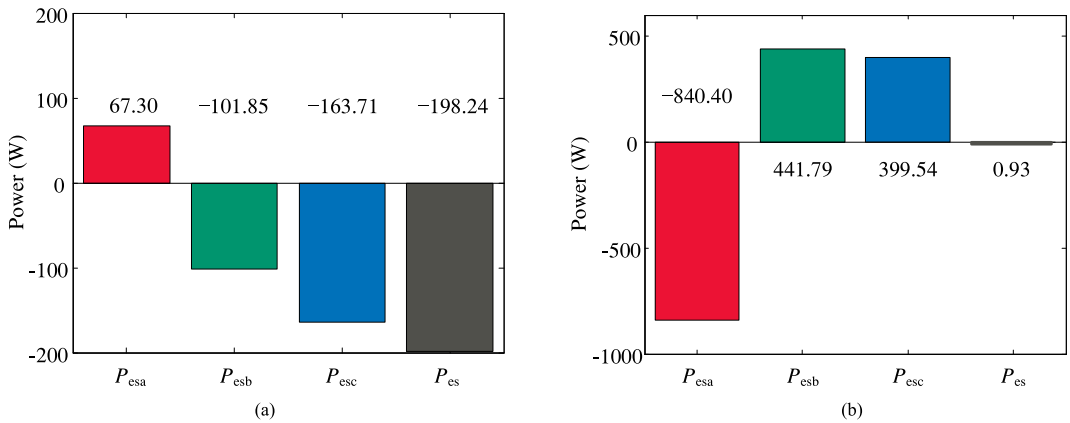

Fig. 16. Total and per-phase active power usage of the ES in case B and case F. (a) The simulation results of the total and per-phase active power usage of the ES in case B with the ES under the RCD control. (b) The simulation results of the total and per-phase active power usage of the ES in case F with the ES under the RCD control.

($P_{es} = P_{esa} + P_{esb} + P_{esc}$) for case B. It indicates that the total active power delivered from the ES to the power system is 198.24 W when the RCD method is employed. The simulated active power of the ES (198.24 W) is closed to the analytical calculation (198.08 W). The simulation results of case F is shown in Fig. 16(b), which shows that the ES delivers nearly zero active power (0.93 W) to the system with the proposed RCD method. This is in line with the analysis in Section III-B. The two simulations verify that the ES active power can be either minimized (in case B) or eliminated (in case F), during the process of restoring power balance under the proposed RCD control method.

C. Experimental Validation

The parameters in case A in Table I are adopted. Both simulation and experiment are performed based on the power stage shown in Fig. 17, where a three-phase three-leg bidirectional power converter is chosen as an ES. In the simulation, the dc bus of the converter is connected to two series-connected ideal

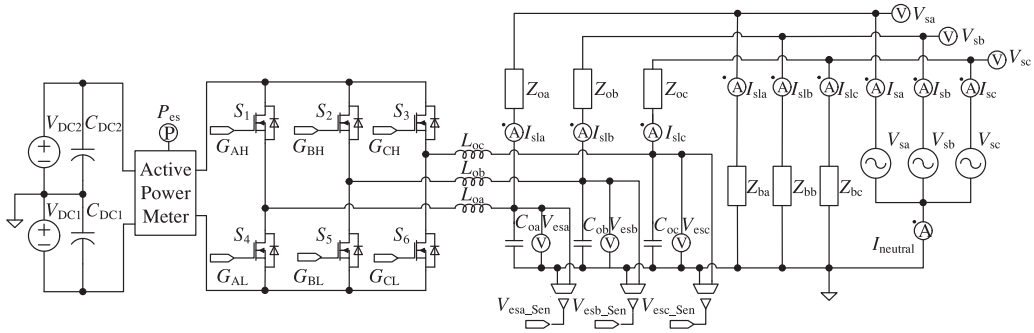

Fig. 17. Power stage of the ES adopted in the PSIM simulation and the experiment in Section IV-B.

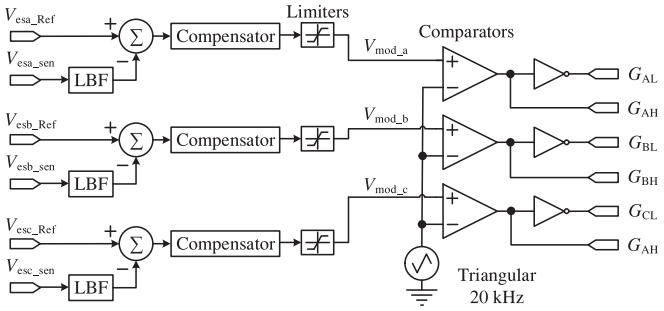

Fig. 18. Control circuit of the ES adopted in the PSIM simulation and the experiment in Section IV-B.

TABLE II
PARAMETERS OF THE SIMULATION AND THE EXPERIMENT IN SECTION IV-C

Description	Parameter	Value
MOSFET switches	S_1–S_6	IRFP31N50L (use ideal NMOS in simulation.)
Storage capacitors	C_1, C_2	6 pcs of 1500-μF capacitors
Filter capacitor	C_{oi}	13.2 μF
Filter inductor	L_{oi}	500 μH
Batteries		LC-R127R2NA (18 pcs in series) (use ideal DC source in simulation.)
Switching frequency	f_{SW}	20 kHz

dc sources V_{DC1} and V_{DC2} and the MOSFET switches S_1–S_6 are configured as ideal NMOS without parasitic resistance and capacitance. The control circuit of the ES adopted in the simulation is shown in Fig. 18. It is connected to the circuit shown in Fig. 9. In the experiment, the two ideal dc sources V_{DC1} and V_{DC2} are realized with 18 units of serially connected 12-V lead-acid batteries. A digital signal processing (DSP) controller Texas Instrument TMS320F28069 is used to implement the control. The control depicted in Figs. 9 and 18 is digitally implemented inside the DSP controller using C programming. The system parameters are given in Table II. The actual experiment setup is shown in Fig. 19.

The simulation and the experiment waveforms of the line and the neutral currents with the ES being deactivated are shown in Fig. 20. The magnitude of the line currents in the experiment are measured using the built-in power analyzer inside the ac power

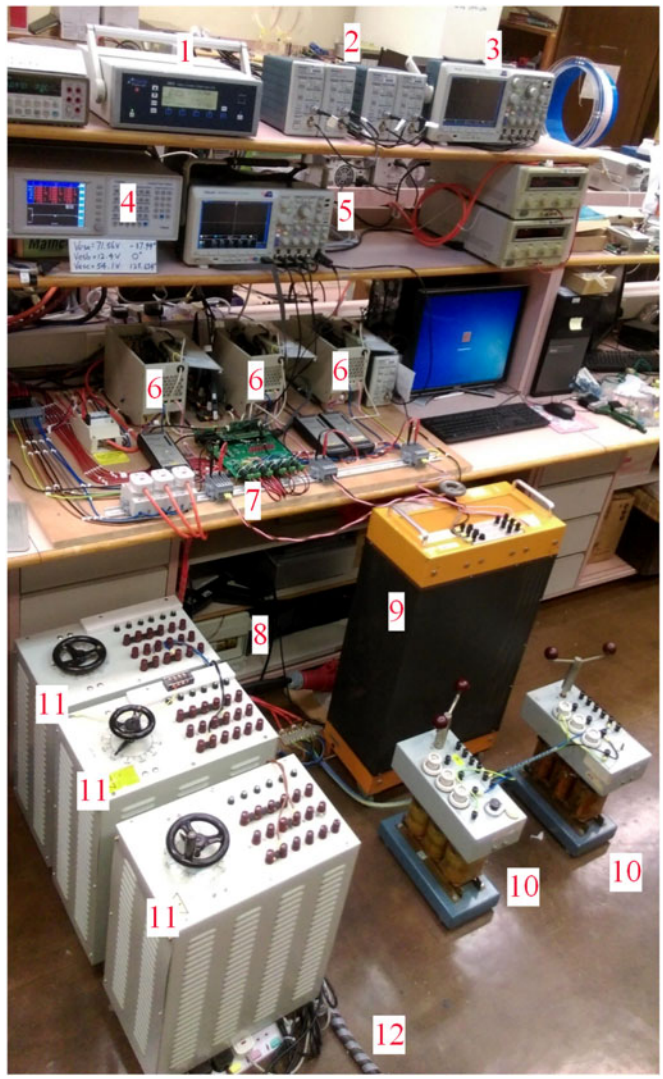

Fig. 19. Actual experimental setup. [1: DC bus power analyzer (XiTRON 2801), 2 and 3: System current measurement setup (Tektronix MSO-3034, Tektronix TCPA300 and Tektronix TCP312) , 4: System power analyzer (Voltech PM6000), 5: ES voltage measurement setup (Tektronix MSO-3034 and Pico Technology TA042), 6: Three-phase eESs, 7: DSP ES controller, 8: Lead-acid battery bank, 9: Resistive NC load banks, 10: Inductive critical loads, 11: Resistive critical load banks, 12: The power cable from the output of the AC power source (California Instruments CSW5550)].

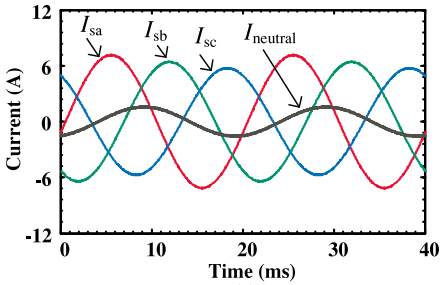

(a)

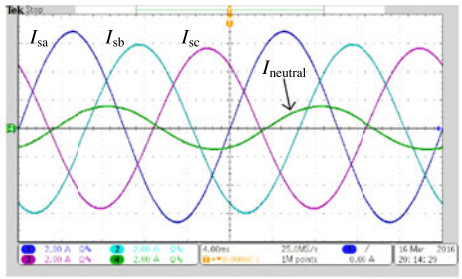

(b)

q (Hz): 50.00	Phase A	Phase B	Phase C
Voltage (V rms):	220.00	220.00	220.00
Current (A rms):	5.121	4.557	4.047
Phase (?:	0.0	240.3	120.6
Power (kW):	1.105	0.996	0.890
Appt.Power (kVA):	1.127	1.003	0.890
Power Factor:	0.98	0.99	1.00
Peak Curr (A): clr	7.259	6.463	5.734
Crest Factor:	1.42	1.42	1.42

(c)

Fig. 20. Simulation and experiment waveforms and the measurement of the system line currents under the deactivation of the ES in case A. (a) Simulation waveforms. (b) Experiment waveforms. (c) Experiment measurement.

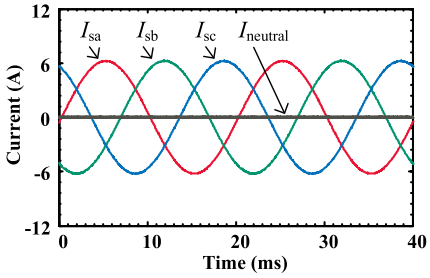

(a)

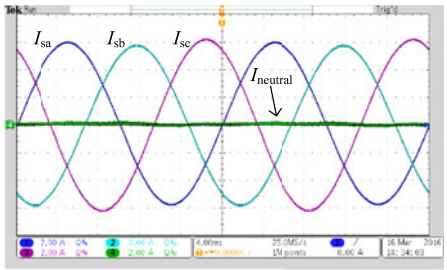

(b)

q (Hz): 50.00	Phase A	Phase B	Phase C
Voltage (V rms):	219.99	219.99	219.99
Current (A rms):	4.484	4.436	4.408
Phase (?:	0.0	240.3	120.6
Power (kW):	0.979	0.969	0.963
Appt.Power (kVA):	0.986	0.976	0.970
Power Factor:	0.99	0.99	0.99
Peak Curr (A): clr	6.356	6.295	6.249

(c)

Fig. 21. Simulation and experiment waveforms and the measurement of the system line currents with the activation of the ES under the RCD control in case A. (a) Simulation waveforms. (b) Experiment waveforms. (c) Experiment measurement.

source (California Instruments CSW5550) and acquired through the Ethernet interface. The readings are shown in Fig. 20(c). It shows $|I_{sa}| = 5.121$ A, $|I_{sb}| = 4.557$ A, and $|I_{sc}| = 4.047$ A. The simulation and experiment waveforms of these line currents are shown in Fig. 20(a) and (b), respectively.

Next, the required ES voltages, according to the proposed RCD method in Section III-B, are calculated as $|V_{esa}|\angle\theta_{esa} = 71.562\angle -0.662$ V, $|V_{esb}|\angle\theta_{esb} = 12.436\angle 0$ V, and $|V_{esc}|\angle\theta_{esc} = 54.150\angle 2.193$ V. The ES is operated with the calculated ES voltage and their voltage waveforms are shown in Fig. 22(a) (simulation) and (b) (experiment). The simulation and experiment line-current and neutral-current waveforms after the activation of the ES is shown in Fig. 21(a) and (b),respectively. Fig. 21(c) shows that the magnitude of the experimentally measured line currents are $|I_{sa}| = 4.484$ A, $|I_{sb}| = 4.436$ A and $|I_{sc}| = 4.408$ A. The measured active and apparent power of the system are $P_{sa} = 979$ W, $P_{sb} = 969$ W, and $P_{sc} = 963$ W and $|S_{sa}| = 986$ VA, $|S_{sb}| = 976$ VA, and $|S_{sc}| = 970$ VA. These active and apparent powers are all nearly equal among the three phases. The results indicate that the neutral current can be mitigated to nearly zero and the line currents can be regulated to be symmetrically balanced. This validates experimentally that the proposed RCD method can achieve three-phase power balancing.

TABLE III
MEASURED ELECTRICAL PARAMETERS OF THE ES

Description	Phase *a*	Phase *b*	Phase *c*
ES RMS voltage (V)	71.427 V	12.559 V	54.181 V
ES RMS current (A)	1.7416 A	2.1258 A	2.5923 A
ES apparent power (VA)	124.4 VA	26.698 VA	140.46 VA
ES power factor	0.6261	0.9983	−0.7437

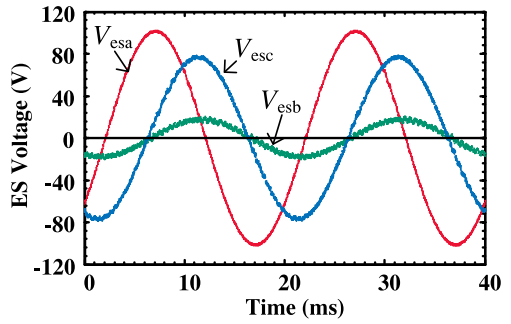

(a)

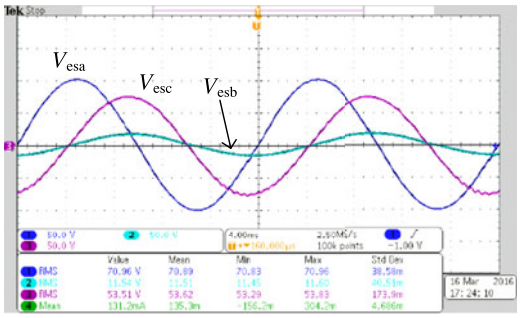

(b)

Fig. 22. Simulation and experiment waveforms of the ES voltages determined by the proposed RCD approach in case A. (a) Simulation waveforms. (b) Experiment waveforms.

The magnitude of the ES voltages, the magnitude of the smart-load currents, the ES apparent power and the power factor of the ES on each phase are measured using a power analyzer (Voltech PM6000). The results are shown in Table III. The total active power delivered by the ES ($P_{\rm es}$) can be calculated as

$$\begin{aligned} P_{\rm es} &= P_{\rm esa} + P_{\rm esb} + P_{\rm esc} \\ &= |S_{\rm esa}|PF_{\rm esa} + |S_{\rm esb}|PF_{\rm esb} + |S_{\rm esc}|PF_{\rm esc} \\ &= 124.4 \times 0.6261 + 26.698 \times 0.9983 \\ &\quad + 140.46 \times (-0.7437) \\ &= 0.079351\,{\rm W} \end{aligned} \tag{34}$$

where $PF_{\rm esa}$, $PF_{\rm esb}$, and $PF_{\rm esc}$ are the power factor of the ES on phase *a*, *b*, and *c*, respectively, and $|S_{\rm esa}|$, $|S_{\rm esb}|$, and $|S_{\rm esc}|$ are the apparent power of the ES on the corresponding phase. The measured ES active power is closed to zero, which confirms that the proposed RCD method can control the ES such that it does not deliver active power to the grid while achieving three-phase power balancing. Note that in the hardware implementation, a certain amount of active power is delivered to the power converter from battery storages to compensate the power loss of the power converter ($P_{\rm es\_loss}$). The amount of active power delivered from batteries ($P_{\rm es\_dc}$) is measured by a power analyzer (Xitron 2801) as $P_{\rm es\_dc} = 21.52$ W. Since the ES is handling 1415-W power (the amount of the three-phase smart-load active power), the power loss of the ES is accounted to be around 1.5% of the smart-load active power. Although the amount of $P_{\rm es\_dc}$ is relatively small, its nonzero value means that a small energy storage is still required. Alternatively, a possible work-around solution is to slightly adjust the phase of the three-phase ES voltage such that $P_{\rm es\_dc}$ can be mitigated to zero. This will result in a slight power imbalance among the three phases, which is typically acceptable in practice.

V. CONCLUSION

This paper presents an in-depth analysis and a control strategy for electric springs (ESs) to mitigate the negative-sequence and the zero-sequence currents in three-phase unbalanced power systems. The proposed control method is based on the radial-chordal decomposition approach, which allows precise calculation of the required ES voltage on each phase such that 1) the ES can restore the power balance and 2) the active power delivered from the battery storage can be minimized. Simulation and experimental results are provided to verify the validity of the proposed control scheme. This method can be potentially developed to include more advanced and multifunctioning controls such as power factor improvement and harmonic elimination.

REFERENCES

[1] B. Blazic and I. Papic, "Improved D-StatCom control for operation with unbalanced currents and voltages," *IEEE Trans. Power Del.*, vol. 21, no. 1, pp. 225–233, Jan. 2006.
[2] D. W. Durbak, "Negative sequence currents from an unbalanced transmission system," in *Power Technology, no. 11. Alpharetta, GA, USA: Siemens Industry Inc.*, Mar. 2012.
[3] V. B. Bhavaraju and P. N. Enjeti, "Analysis and design of an active power filter for balancing unbalanced loads," *IEEE Trans. Power Electron.*, vol. 8, no. 4, pp. 640–647, Oct. 1993.
[4] A. Chandra, B. Singh, B. N. Singh, and K. Al-Haddad, "An improved control algorithm of shunt active filter for voltage regulation, harmonic elimination, power-factor correction, and balancing of nonlinear loads," *IEEE Trans. Power Del.*, vol. 15, no. 3, pp. 495–507, May 2000.
[5] S. George and V. Agarwal, "A DSP based optimal algorithm for shunt active filter under nonsinusoidal supply and unbalanced load conditions," *IEEE Trans. Power Electron.*, vol. 22, no. 2, pp. 593–601, Mar. 2007.
[6] S. Yan, S. C. Tan, C. K. Lee, B. Chaudhuri, and S. Y. R. Hui, "Electric springs for reducing power imbalance in three-phase power systems," *IEEE Trans. Power Electron.*, vol. 30, no. 7, pp. 3601–3609, Feb. 2015.
[7] N. Johansson, L. Angquist, and H. P. Nee, "An adaptive controller for power system stability improvement and power flow control by means of a thyristor switched series capacitor (TSSC)," *IEEE Trans. Power Syst.*, vol. 25, no. 1, pp. 381–391, Feb. 2010.
[8] B. Singh, K. Al-Haddad, and A. Chandra, "A review of active filters for power quality improvement," *IEEE Trans. Ind. Electron.*, vol. 46, no. 5, pp. 960–971, Oct. 1999.
[9] C. Vournas and M. Karystianos, "Load tap changers in emergency and preventive voltage stability control," *IEEE Trans. Power Syst.*, vol. 19, no. 1, pp. 492–498, Feb. 2004.
[10] S. Y. Lee and C. J. Wu, "Reactive power compensation and load balancing for unbalanced three-phase four-wire system by a combined system of an SVC and a series active filter," *Proc. IEE*, vol. 147, no. 6, pp. 563–578, Nov. 2000.

[11] P. Verdelho and G. D. Marques, "An active power filter and unbalanced current compensator," *IEEE Trans. Ind. Electron.*, vol. 44, no. 3, pp. 321–328, Jun. 1997.
[12] A. Ghosh and A. Joshi, "A new approach to load balancing and power factor correction in power distribution system," *IEEE Trans. Power Del.*, vol. 15, no. 1, pp. 417–422, Jan. 2000.
[13] L. Gyugyi, C. D. Schauder, and K. K. Sen, "Static synchronous series compensator: A solid-state approach to the series compensation of transmission lines," *IEEE Trans. Power Del.*, vol. 12, no. 1, pp. 406–417, Jan. 1997.
[14] A. Hasanzadeh, M. Parniani, and S. M. R. Sadriyeh, "A comparative study on current control methods for load balancing and power factor correction using STATCOM," in *Proc.IEEE Russia Power Tech*, Jun. 2005, pp. 1–7.
[15] L. Gyugyi, C. D. Schauder, S. L. Williams, T. R. Rietman, D. R. Torgerson, and A. Edris, "The unified power flow controller: A new approach to power transmission control," *IEEE Trans. Power Del.*, vol. 10, no. 2, pp. 1085–1097, Apr. 1995.
[16] T. Isobe, D. Shiojima, K. Kato, Y. R. R. Hernandez, and R. Shimada, "Full-bridge reactive power compensator with minimized-equipped capacitor and its application to static VAR compensator," *IEEE Trans. Power Electron.*, vol. 31, no. 1, pp. 224–234, Jan. 2016.
[17] H. Akagi and H. Fujita, "A new power line conditioner for harmonic compensation in power systems," *IEEE Trans. Power Del.*, vol. 10, no. 3, pp. 1570–1575, Jul. 1995.
[18] F. F. Wu, P. P. Varaiya, and S. Y. R. Hui, "Smart grids with intelligent periphery: An architecture for the energy internet," *Engineering*, vol. 1, no. 4, pp. 436–446, Dec. 2015.
[19] S. Y. R. Hui, C. K. Lee, and F. F. Wu, "Electric springs—A new smart grid technology," *IEEE Trans. Smart Grid*, vol. 3, no. 3, pp. 1552–1561, Sep. 2012.
[20] S. C. Tan, C. K. Lee, and S. Y. R. Hui, "General steady-state analysis and control principle of electric springs with active and reactive power compensations," *IEEE Trans. Power Electron.*, vol. 28, no. 8, pp. 3958–3969, Aug. 2013.
[21] P. Kanjiya and V. Khadkikar, "Enhancing power quality and stability of future smart grid with intermittent renewable energy sources using electric springs," in *Proc.IEEE Renew. Energy Res. Appl.*, Oct. 2013, pp. 918–922.
[22] P. B. Darji and A. M. Kulkarni, "Vector definitions for control of single-phase and unbalanced three-phase systems," *IEEE Trans. Power Del.*, vol. 29, no. 5, pp. 2136–2145, Oct. 2014.
[23] S. Li, Y. Li, J. Sun, Q. Jin, and X. Li, "A novel control algorithm for inverter-based distributed generation in unbalanced three-phase power systems," in *Proc. IEEE Int. Conf. Sustain. Power Gener. Supply*, Apr. 2009, pp. 1–6.
[24] *Rotating Electrical Machines Part 1: Rating and Performance*, International Electrotechnical Commission (IEC) Standard, EN 60034-1, 2010.
[25] J. S. Lai and T. S. Key, "Effectiveness of harmonic mitigation equipment for commercial office buildings," *IEEE Trans. Ind. Appl.*, vol. 33, no. 4, pp. 1104–1110, Jul. 1997.
[26] K. T. Mok, S. C. Tan, and S. Y. R. Hui, "Decoupled power angle and voltage control of electric springs," *IEEE Trans. Power Electron.*, vol. 31, no. 2, pp. 1216–1229, Feb. 2016.
[27] G. Strang, *Calculus*. Wellesley, MA, USA: Wellesley-Cambridge Press, 1991. [Online]. Available: https://books.google.com.hk/books?id=OisInC1zvEMC

Kwan-Tat Mok (S'14–16) received the B.Eng. (Hons.) and M.Phil. degrees in electronic and information engineering from the Hong Kong Polytechnic University, Hong Kong, in 2009 and 2012, respectively, and the Ph.D. degree in electrical and electronic engineering from The University of Hong Kong, Hong Kong, in 2016.

In 2007, he worked as an Engineering Trainee in Solomon Systech Ltd., Hong Kong, for a one-year internship program. From September 2011 to February 2013, he was an Embedded System Engineer, Cwlinux Limited, Hong Kong. From July to August 2015, he was a visiting postgraduate student in Department of Electrical and Electronic Engineering, Imperial College London. He is currently a Research Associate in Power Electronics Research Group, Department of Electrical and Electronic Engineering, The University of Hong Kong. His research interests include smart grid technologies, electric springs, and power converters for light-emitting diodes.

Siu-Shing Ho received the B.Eng. (Hons.) degree in electronic engineering from the City University of Hong Kong, Kowloon Tong, Hong Kong, in 2008.

From 1996 to 2006, he was an Electronic Engineer in the Astec Custom Power (HK) LTD. He is currently a Research Associate in Power Electronics Research Group, University of Hong Kong, Hong Kong. His research interests include control of power electronics and smart grid.

Siew-Chong Tan (M'06–SM'11) received the B.Eng. (Hons.) and M.Eng. degrees in electrical and computer engineering from the National University of Singapore, Singapore, in 2000 and 2002, respectively, and the Ph.D. degree in electronic and information engineering from the Hong Kong Polytechnic University, Hong Kong, in 2005.

From October 2005 to May 2012, he worked as a Research Associate, a Postdoctoral Fellow, a Lecturer, and an Assistant Professor in the Department of Electronic and Information Engineering, Hong Kong Polytechnic University. From January to October 2011, he was a Senior Scientist with Agency for Science, Technology and Research (A*Star), Singapore. He is currently an Associate Professor in the Department of Electrical and Electronic Engineering, The University of Hong Kong, Hong Kong. He was a Visiting Scholar with Grainger Center for Electric Machinery and Electromechanics, University of Illinois at Urbana-Champaign, Champaign, IL, USA, from September to October 2009, and an Invited Academic Visitor of the Huazhong University of Science and Technology, Wuhan, China, in December 2011. He is a coauthor of the book *Sliding Mode Control of Switching Power Converters: Techniques and Implementation* (Boca Raton, FL, USA: CRC, 2011).His research interests are focused in the areas of power electronics and control, LED lightings, smart grids, and clean energy technologies.

Dr. Tan serves extensively as a Reviewer for various IEEE/IET transactions and journals on power, electronics, circuits, and control engineering. He is an Associate Editor of the IEEE TRANSACTIONS ON POWER ELECTRONICS.

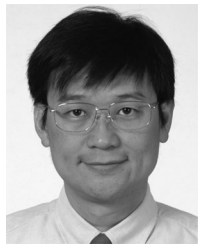

S. Y. (Ron) Hui (M'87–SM'94–F'03) received the B.Sc. (Eng.) (Hons.) from the University of Birmingham, Birmingham, U.K., in 1984 and the D.I.C. and Ph.D. degrees from Imperial College London, London, U.K., in 1987.

He currently holds the Philip Wong Wilson Wong Chair Professorship at the University of Hong Kong, Hong Kong, and a part-time Chair Professorship at Imperial College London. He has published more than 300 technical papers, including more than 220 refereed journal publications. More than 60 of his patents have been adopted by industry.

Dr. Hui is an Associate Editor of the IEEE TRANSACTIONS ON POWER ELECTRONICS and the IEEE TRANSACTIONS ON INDUSTRIAL ELECTRONICS, and an Editor of the IEEE JOURNAL OF EMERGING AND SELECTED TOPICS IN POWER ELECTRONICS. His inventions on wireless charging platform technology underpin key dimensions of Qi, the world's first wireless power standard, with freedom of positioning and localized charging features for wireless charging of consumer electronics. He received the IEEE Rudolf Chope R&D Award from the IEEE Industrial Electronics Society and the IET Achievement Medal (The Crompton Medal) in 2010, and IEEE William E. Newell Power Electronics Award in 2015. He is a Fellow of the Australian Academy of Technological Sciences & Engineering and also the Royal Academy of Engineering, U.K.